Atmospheric Radiative Processes Accelerate Ground Surface Warming over the Southeastern Tibetan Plateau during 1998–2013

PENG JI

Key Laboratory of Regional Climate-Environment for Temperate East Asia, Institute of Atmospheric Physics, Chinese Academy of Sciences, and College of Earth and Planetary Sciences, University of Chinese Academy of Sciences, Beijing, China

XING YUAN

Key Laboratory of Regional Climate-Environment for Temperate East Asia, Institute of Atmospheric Physics, Chinese Academy of Sciences, Beijing, and School of Hydrology and Water Resources, Nanjing University of Information Science and Technology, Nanjing, China

DAN LI

Department of Earth and Environment, Boston University, Boston, Massachusetts

(Manuscript received 2 June 2019, in final form 17 November 2019)

ABSTRACT

The Tibetan Plateau (TP), known as the world's ''Third Pole,'' plays a vital role in regulating the regional and global climate and provides freshwater for about 1.5 billion people. Observations show an accelerated ground surface warming trend over the southeastern TP during the global warming slowdown period of 1998–2013, especially in the summer and winter seasons. The processes responsible for such acceleration are under debate as contributions from different radiative processes are still unknown. Here we estimate for the first time the contributions of each radiative component to the ground surface warming trend before and after 1998 by analyzing multisource datasets under an energy balance framework. Results show that declining cloud cover caused by the weakening of both the South Asian summer monsoon and local-scale atmospheric upward motion mainly led to the accelerated ground surface warming during the summers of 1998–2013, whereas the decreased surface albedo caused by the snow melting was the major warming factor in winter. Moreover, increased clear-sky longwave radiation induced by the warming middle and upper troposphere was the second largest factor, contributing to about 21%–48% of the ground surface warming trend in both the summer and winter seasons. Our results unravel the key processes driving the ground surface warming over the southeastern TP and have implications for the development of climate and Earth system models in simulating ground surface temperature change and other related complex cryosphere–hydrosphere–atmosphere interactions over high-altitude land areas.

1. Introduction

Located in central Asia, the Tibetan Plateau (TP) is the highest plateau in the world (Bird and Toksöz 1977; Qiu 2008) and has profound influences on the regional and global climate (Duan and Wu 2009; Lin and Wu 2011; Xue et al. 2017). The TP has Earth's third largest store of ice, with more than 1×10^5 km^2 of glaciers and about 1.73×10^6 km^2 of permafrost (Yang et al. 2010; Yao et al. 2012), making it known as the ''Third Pole'' (Qiu 2008). Over the past few decades, the TP has seen significant increases in the ground surface temperature (Fang et al. 2019; Zhu et al. 2018), resulting in permafrost degradation, snow melting, glacier shrinking, and other related hydrological changes (Dehecq et al. 2019; Ji and Yuan 2018; Yang et al. 2010; Yang et al. 2014). In addition, the ground surface warming propagates into deeper soil

Supplemental information related to this paper is available at the Journals Online website: https://doi.org/10.1175/JCLI-D-19-0410.s1.

Corresponding author: Xing Yuan, xyuan@nuist.edu.cn

DOI: 10.1175/JCLI-D-19-0410.1

layers, which further accelerates soil respiration (Ma et al. 2018) and modifies the distribution of soil crust microbial communities (Garcia-Pichel et al. 2013). In cold regions such as the TP, soil temperature changes are critical for biogeochemical processes due to the high sensitivity of soil carbon turnover to soil temperature (Koven et al. 2017).

Although the ground surface temperature is tightly coupled with the surface air temperature, they can change in different ways especially in cold regions (Brown and Degaetano 2011; Woodbury et al. 2009). Recent research demonstrates the necessity to focus on soil temperature instead of air temperature when predicting changes in soil carbon release in a changing climate due to their different warming trends (Zhang et al. 2016). Thus, the spatiotemporal variations and the long-term changes of soil temperature over the TP at both the surface and the subsurface have been receiving more attention (Fang et al. 2019; Wang et al. 2018; Zhu et al. 2018). The annual mean ground surface temperature over the TP increased at a rate of 0.7°C decade^{-1} during 1983–2013, which is 1.4 times the annual mean surface air temperature warming rate (Zhu et al. 2018). Even during 1998–2013 when the global temperature warming trend slowed down (Kosaka and Xie 2013; Medhaug et al. 2017; Xie and Kosaka 2017), the ground surface temperature over TP continued to increase (Wang et al. 2018).

A key factor responsible for the continued ground surface warming trend over the TP is the snow–albedo feedback; that is, the decreased snow cover under warmer conditions can cause the surface albedo to reduce, thereby further warming the ground (Ghatak et al. 2014). Recent research highlights the importance of light-absorbing aerosols deposition such as organic carbon and mineral dust in reducing the surface albedo and warming the ground surface (He et al. 2018; Ramanathan and Carmichael 2008). However, less attention has been paid to changes in atmospheric radiative processes and turbulent heat fluxes. Previous work suggests that the cloud cover over the southern TP decreased during 1998–2009, which increased surface shortwave radiation and contributed to the continued warming over the TP (Duan and Xiao 2015), but the quantitative contribution of this process to the ground surface warming trend is still unknown. Moreover, the sensible heat flux has increased since the beginning of the twenty-first century (Zhu et al. 2017), but to what extent it has cooled the ground surface remains to be quantified. In summary, there is still no quantitative analysis on the contributions from different radiative processes to the continued ground surface warming over TP during the global warming slowdown period of 1998–2013, and whether their contributions change over time remains unknown.

In this study, we first show that the ground surface warming trend over the southeastern TP accelerated during 1998–2013, relative to 1981–97, especially in the summer and winter seasons. We then quantify the contributions of surface albedo, different atmospheric radiative processes, and turbulent heat fluxes to the ground surface warming trends before and after 1998, followed by explaining the physical mechanisms responsible for the changes in atmospheric radiative forcings.

2. Data and methods

a. *Observational, reanalysis, and remote sensing-based datasets*

Monthly ground surface temperature observations from 1089 China Meteorological Administration (CMA) stations (http://data.cma.cn/en) during 1981–2013 are used in this study, with 121 of them located over the TP. Daily total cloud fraction observations during 1981–2009 are obtained from the Carbon Dioxide Information Analysis Center Extended Edited Cloud Reports Archive (CDIAC-EECRA; Hahn et al. 1999).

Monthly ground surface temperature during 1981–2013 from the Modern-Era Retrospective Analysis for Research and Applications (MERRA; Rienecker et al. 2011) and MERRA, version 2 (MERRA2; Gelaro et al. 2017) from the National Aeronautics and Space Administration (NASA) Goddard Earth Science Data Information and Services Center, the Japanese 55-year Reanalysis (JRA-55; Kobayashi et al. 2015) from the Japan Meteorological Agency, and the European Centre for Medium-Range Weather Forecasts interim reanalysis (ERA-Interim; Dee et al. 2011) are used. Spatial resolutions are 0.5° × 0.667° for MERRA and MERRA2, TL319 (~55 km) for JRA-55, and 0.75° × 0.75° for ERA-Interim.

Surface radiative datasets based on radiative transfer model and satellite retrieval data are also used, including the NASA/GEWEX Surface Radiation Budget both using detailed radiative transfer algorithm (GEWEX-SRB; Pinker and Laszlo 1992) and a fast parameterization algorithm (GEWEX-LPLA; Gupta et al. 2001) during 1984–98, the International Satellite Cloud Climatology Project-FD (ISCCP-FD; Zhang et al. 2004) during 1984–98, and Clouds and the Earth's Radiant Energy System (CERES; Kato et al. 2018) during 2001–13. Spatial resolutions are 1.0° × 1.0° for GEWEX-SRB, GEWEX-LPLA, and CERES, with a 280-km equal-area grid for ISCCP-FD. Note that the sums of latent and sensible heat fluxes are not provided by those remote sensing-based datasets, so they are estimated through the surface energy balance equation assuming a

zero ground heat flux. Moreover, monthly total cloud fraction from CERES during 2000–13 is also used to investigate cloud changes, considering that CDIAC-EECRA only extends to 2009.

b. *High-resolution regional climate and offline land surface simulations*

We use the Weather Research and Forecasting (WRF) mesoscale model (Skamarock et al. 2008) to conduct a long-term simulation at 30-km resolution during 1980–2014 to provide a high-resolution dataset. The model domain covers all of China with 195 × 158 grid points in each of the zonal and meridional directions. There are 30 vertical layers and the top of the model is 50 hPa. ERA-Interim data are used to provide the initial and lateral boundary conditions. The time step of integration interval is 180 s. Before doing the long-term simulation, we tested the performance of six physical configurations during the wet (1998) and dry (2006) years of TP. The combination of the Grell–Devenyi ensemble cumulus parameterization scheme and the RRTMG radiation scheme was finally chosen according to the best performance in simulating the monthly temperature over China including the TP (see Fig. S1 in the online supplemental material). Other model physics include the WRF single-moment three-class cloud microphysics scheme, the Yonsei University planetary boundary layer scheme, and the Noah land surface model.

We use the China Meteorological Forcing Dataset (CMFD; He and Yang 2011) to drive the Conjunctive Surface-Subsurface Process version 2 (CSSPv2; Yuan et al. 2018) land surface model at 10-km resolution over TP during 1979–2014 to provide another high-resolution dataset (hereafter referred to as CMFD/CSSPv2). Previous study shows that the CMFD/CSSPv2 captures the ground surface temperature variation and its long-term changes well (Yuan et al. 2018). CMFD/CSSPv2 cannot distinguish clear-sky radiation and cloudy-sky radiation from total-sky radiation, but the attribution results by using CMFD/CSSPv2 can indicate the overall importance of shortwave and longwave radiation, which makes the results more robust especially during winter (see section 3c).

c. *Separation of contributions based on the energy balance equation*

The perturbation form of surface energy balance equation at monthly scale over land surface is used to separate contributions from different radiative processes (Lesins et al. 2012; Lu and Cai 2009). The perturbed energy balance equation can be written as

$$\Delta F^{\uparrow} = \Delta\varepsilon F^{\downarrow} + \Delta[(1-\alpha)S^{\downarrow}] - \Delta(H + \mathrm{LE}) - \Delta G, \quad (1)$$

where Δ is difference between two months, $F^{\uparrow}$ and $F^{\downarrow}$ are upward and downward longwave radiation, ε is ground emissivity, $S^{\downarrow}$ is downward shortwave radiation, α represents surface albedo, H and LE represent sensible and latent heat flux, respectively, and G is the ground heat flux. To separate the cloud effects, Eq. (1) can be further expanded as

$$4\sigma\overline{\varepsilon}\,\overline{T_s}^{3}\Delta T_s \approx \Delta F_s^{\uparrow} = \left\{ \begin{array}{l} \underbrace{-(\Delta\alpha)(\overline{S^{\downarrow}} + \Delta S^{\downarrow})}_{\text{Surface albedo change}} + \underbrace{(1-\overline{\alpha})\,\Delta S^{\downarrow,\mathrm{cld}} + \overline{\varepsilon}\Delta F^{\downarrow,\mathrm{cld}}}_{\text{Cloud-radiative forcing}} + \underbrace{(1-\overline{\alpha})\,\Delta S^{\downarrow,\mathrm{clr}}}_{\substack{\text{Clear-sky shortwave}\\ \text{radiation change}}} + \underbrace{\overline{\varepsilon}\,\Delta F^{\downarrow,\mathrm{clr}}}_{\substack{\text{Clear-sky longwave}\\ \text{radiation change}}} \\ \\ \underbrace{-\Delta(H + \mathrm{LE})}_{\substack{\text{Surface turblent}\\ \text{fluxes changes}}} \underbrace{-\Delta G}_{\substack{\text{Ground heat}\\ \text{flux change}}} \end{array} \right\}, \quad (2)$$

where σ is the Stefan–Boltzmann constant, and T_s is ground surface temperature with the overbar denoting a mean state. Also, $S^{\downarrow,\mathrm{cld}}$ and $S^{\downarrow,\mathrm{clr}}$ represent cloudy-sky and clear-sky shortwave radiations respectively, while $F^{\downarrow,\mathrm{cld}}$ and $F^{\downarrow,\mathrm{clr}}$ are cloudy-sky and clear-sky longwave radiations, respectively.

Using Eq. (2), ground surface temperature of a specific month i can be expressed as follows:

$$\begin{aligned} T_{s,i} \approx T_0 + \sum_{t=1}^{i} \frac{1}{4\sigma\overline{\varepsilon}\,\overline{T_{s,t}}^{3}} \{ & -(\Delta\alpha_t)(\overline{S^{\downarrow}}_{t-1} + \Delta S_t^{\downarrow}) \\ & + (1-\overline{\alpha_{t-1}})\Delta S_t^{\downarrow,\mathrm{cld}} + \Delta F_t^{\downarrow,\mathrm{cld}} + (1-\overline{\alpha_{t-1}})\Delta S_t^{\downarrow,\mathrm{clr}} \\ & + \Delta F_t^{\downarrow,\mathrm{clr}} - \Delta G_t - \Delta(H + \mathrm{LE})_t \}, \end{aligned} \quad (3)$$

where T_0 is the initial temperature. Ground temperature time series can be separated into different components

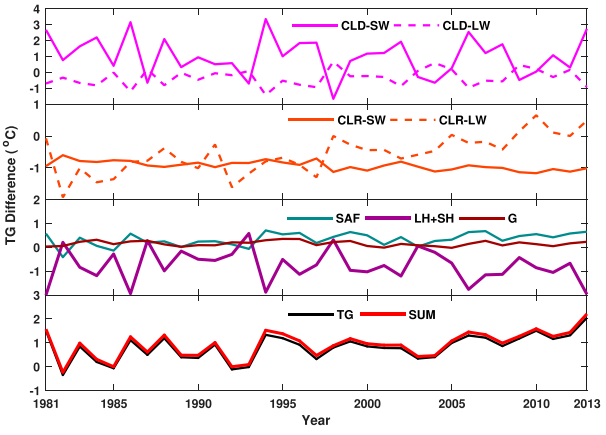

FIG. 1. Example of the decomposition of ground surface temperature difference. Ground surface temperature (TG) difference time series during 1981–2013 are separated into different parts including contributions from surface albedo change (SAF), cloud shortwave and longwave effects (CLD-SW and CLD-LW), clear-sky shortwave and longwave effects (CLR-SW and CLR-LW), latent and sensible heat flux (LH + SH), ground heat flux (G), and their sum (SUM). The differences are relative to TG in 1980. The dataset used here is from the WRF simulation.

using Eq. (3) as shown in Fig. 1. The linear trend of ground temperature can thus be attributed to different processes. Generally, the trend estimated by Eq. (3) is not necessarily the same as the actual value, but the bias is very small. For the example shown in Fig. 1, the ground temperature changing rates during 1981–97 and 1998–2013 are 0.09° and 0.59°C decade^{-1}, while the estimated rates are 0.13° and 0.61°C decade^{-1}, respectively.

d. *Stepwise regression of clear-sky longwave radiation*

We use the following equation to describe the relation between clear-sky longwave radiation (CLR − LW), air temperature at different layers (T_z) over troposphere (850–200 hPa), and precipitable water (PW):

$$\mathrm{CLR}-\mathrm{LW}=a+\sum_{z=1}^{n}b_zT_z^4+c\mathrm{PW}^d+\sum_{z=1}^{n}e_zT_z^4\mathrm{PW}^d, \tag{4}$$

where the first term is the intercept, the second term represents contribution from longwave radiation emitted from different air layers, the third term is the water vapor effect, and the last term represents their interaction. The coefficients are determined following two steps. First, factor d is determined by fitting a power-law function between CLR − LW and PW. Second, the linear stepwise regression method is used to determine other coefficients. We choose stepwise regression mainly because the factors are not independent, and only factors with significant contributions should be included. Performance of regression does not increase and even decreases when we consider the interaction of longwave radiation at different layers by adding the interaction terms $\sum_{z,k=1;z\neq k}^{n}b_{z,k}(T_z^4T_k^4)$, and thus we do not consider this interaction in the regression function. The differential form of Eq. (4) is used to estimate different contributions from air temperature change and water vapor change to the clear-sky longwave radiation change.

e. *Study domain and uncertainty estimation*

For regions like the TP where the topography is complex and observation stations are usually located in valleys and close to the towns in the eastern part, it is not appropriate to extend the evaluation results based on the station observations to the whole TP (Yang et al. 2008). Thus we mainly focus on the southeastern TP (green dashed lines in Fig. 2; 26°–35°N, 90°–105°E), where the observation stations are dense and gridded datasets have a relatively good performance (see section 3b).

Model outputs at those grids closest to the observation stations are extracted, and are averaged for regional analysis. Then Eq. (3) is used to separate contributions from different radiative factors. The linear trend and its significance are calculated by using the ordinary least squares method (OLS) and the two-tailed Student's t test, respectively.

A comparison between different state-of-the-art reanalysis datasets helps make robust assessments and quantify uncertainties (Rienecker et al. 2011), so we intercompare the reanalysis datasets, remote sensing–based datasets, and WRF and CMFD/CSSPv2 simulations to ensure robustness of the attribution results in this study. Different datasets are treated equally without any priority, and only those datasets that capture the ground warming trend will be finally chosen. Attribution analysis is conducted separately for the chosen datasets and the contribution from a specific factor will be considered detectable when the ensemble mean of the attribution results is larger than the uncertainty (e.g., one standard deviation among different datasets). The uncertainty of each dataset due to sampling is estimated by a bootstrapping method (10 000 times) for the 90% stations.

3. Results

a. *Accelerated ground surface warming over the Tibetan Plateau*

As shown in Fig. 2a, ground surface temperature trends averaged over southeastern TP during 1981–97

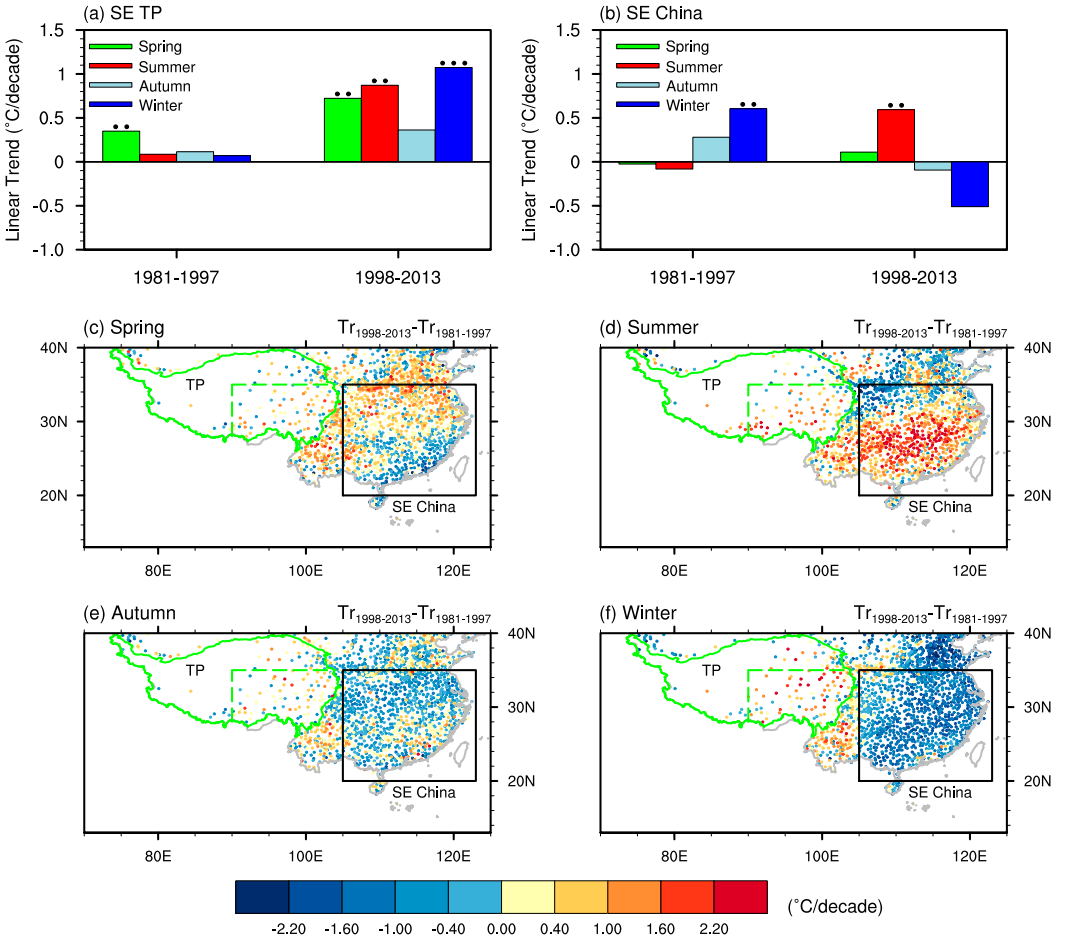

FIG. 2. (a) Linear trends of spatial mean ground surface temperature over the southeastern Tibetan Plateau during different seasons of 1981–97 and 1998–2013. (b) As in (a), but for southeastern China. Two dots and three dots indicate significance at the 95% and 99% confidence levels, respectively. (c)–(f) Changes of linear trends for each station during 1998–2013 compared with that during 1981–97 in different seasons. The green solid line in (c)–(f) is the boundary of the Tibetan Plateau; the green dashed line shows the boundary of the southeastern TP.

are 0.35°C decade^{-1} (p = 0.02), 0.09°C decade^{-1} (p = 0.35), 0.11°C decade^{-1} (p = 0.31), and 0.07°C decade^{-1} (p = 0.4) in spring (March–May), summer (June–August), autumn (September–December), and winter (December–February), respectively. However, the warming rates during 1998–2013 increase to 0.72°C decade^{-1} (p = 0.02), 0.87°C decade^{-1} (p = 0.01), 0.36°C decade^{-1} (p = 0.13), and 1.07°C decade^{-1} ($p < 0.01$), respectively. The Mann–Kendall test is also used to test the significance of the warming trend during 1998–2013, and the result is consistent with the Student's t test (not shown). Thus, accelerated ground surface warming over southeastern TP during 1998–2013 is robust and convincing. In addition, warming rate changes are 0.78° and 1.0°C decade^{-1} in summer and winter respectively, which are much larger than that in spring (0.37°C decade^{-1}) and autumn (0.25°C decade^{-1}). This indicates that accelerated warming is more obvious in summer and winter seasons.

As a comparison, over southeastern (SE) China at the same latitudes, the ground surface warming trend increases from −0.08°C decade^{-1} (p = 0.60) to 0.59°C decade^{-1} (p = 0.02) in summer (Fig. 2b). That is, SE China also experiences accelerated ground surface warming in summer. However, a ground surface cooling occurs in winter over SE China during 1998–2013 as the trend decreases from 0.60°C decade^{-1} (p = 0.05) to −0.51°C decade^{-1} (p = 0.13) (Fig. 2b), which is contrary to the accelerated warming over the southeastern TP.

Spatially, stations with accelerated ground surface warming are mainly located over the southeastern TP in spring, summer, and autumn (Figs. 2c–e), whereas nearly the entire TP shows an accelerated warming trend in winter (Fig. 2f). Duan and Xiao (2015) also

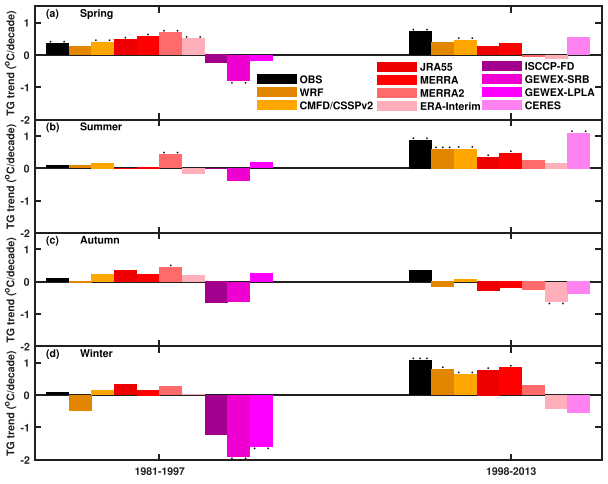

FIG. 3. (a) Linear trends of observed and simulated spring ground temperature (TG) averaged among 78 stations over the southeastern Tibetan Plateau. (b)–(d) As in (a), but for the summer, autumn, and winter seasons, respectively. One dot, two dots, and three dots indicate significance at the 90%, 95%, and 99% confidence levels, respectively. The analysis periods for the trends are 1984–97 for ISCCP-FD, GEWEX-SRB, and GEWEX-LPLA, and 2001–13 for CERES due to the availability of satellite data.

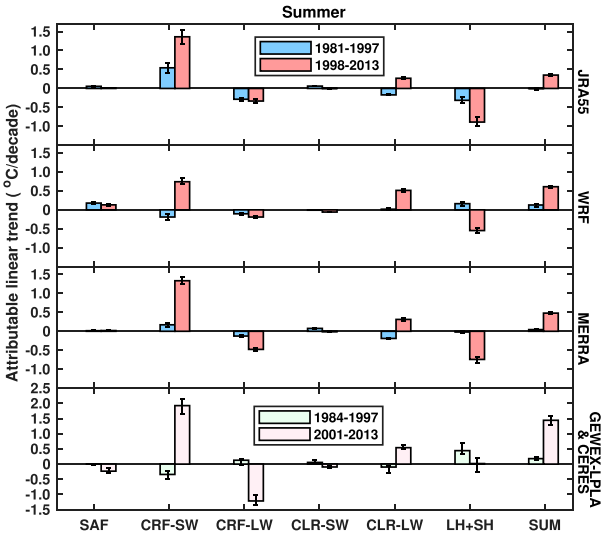

FIG. 4. Contributions from surface albedo (SAF), cloud shortwave and longwave radiation (CRF-SW and CRF-LW), clear-sky shortwave and longwave radiation (CLR-SW and CLR-LW), and latent and sensible heat flux (LH + SH) during 1981–97 and 1998–2013 in the summer seasons. The contribution from ground heat flux is much smaller and is not shown here. "SUM" means integrated trends from all radiative factors. Black bars represent sampling uncertainties at the 95% confidence level.

found a similar phenomenon for surface air temperature, but the increasing trend of ground surface temperature shown here is much larger and more significant.

b. *Evaluations of different datasets*

We evaluate the performances of WRF Model simulation, CMFD/CSSPv2, four atmospheric reanalysis datasets (JRA-55, ERA-Interim, MERRA, and MERRA2), and four remote sensing–based datasets (ISCCP-FD, GEWEX-SRB, GEWEX-LPLA, and CERES) for capturing the accelerated ground warming trend phenomenon over the southeastern TP. Figure 3 shows that only CMFD/CSSPv2 can capture the significant warming in spring during 1998–2013. For the summer and winter seasons, the WRF Model simulation, CMFD/CSSPv2, JRA-55, and MERRA can capture the changes of ground surface warming rate reasonably, although they underestimate the warming trend during the second period. MERRA2 fails to capture the accelerated warming, as the estimated warming rates during 1998–2013 in summer and winter are both less than those during 1981–97. ERA-Interim shows insignificant warming in summer and even a cooling trend in winter during 1998–2013. Hence neither MERRA2 nor ERA-Interim is chosen in the attribution analysis. For remote sensing–based datasets, GEWEX-LPLA better captures the warming trend in summer during 1984–97 as compared to GEWEX-SRB and the ISCCP-FD. The CERES dataset shows a similar warming trend as observations during summer of 2001–13, but it shows insignificant ground temperature changes in winter season. Based on the evaluation results, we mainly focus on the summer and winter seasons in the following analysis, and remote sensing–based datasets are only used for the attribution analysis in summer.

c. *Contributions from different processes*

Contribution results are generally consistent for JRA-55, WRF, and MERRA in summer especially during 1998–2013 (Fig. 4). The surface albedo (SAF) and clear-sky shortwave radiation (CLR-SW) do not make large contributions and show small differences between the two periods. In contrast, surface downward cloudy-sky shortwave radiation shows a much larger increasing trend during 1998–2013 than during 1981–97 (Fig. S2a). Although the surface downward cloudy-sky longwave radiation decreases during 1998–2013, the decreasing rate is smaller than the increasing trend of cloudy-sky shortwave radiation. Thus, the contribution from total cloud-radiative forcing (CRF-SW + CRF-LW) increases significantly from −0.29°–0.26°C decade^{-1} during 1981–97 to 0.55°–1.03°C decade^{-1} during 1998–2013 (Fig. 4). Clear-sky longwave radiation (CLR-LW) shows little change during 1981–97 (Fig. S2a), which only changes the ground surface temperature trend by −0.19°–0.02°C decade^{-1} (Fig. 4). However, clear-sky longwave radiation increases during 1998–2013 (Fig. S2a), leading to a warming rate of 0.27°–0.5°C decade^{-1} (Fig. 4). In

contrast to the cloud-radiative forcing and clear-sky longwave radiation, the sensible and latent heat fluxes play a cooling role during 1998–2013 as their cooling contribution increases from a range of −0.31° to 0.16°C decade^{-1} to a range of −0.54° to −0.89°C decade^{-1}. The ensemble results for total cloud-radiative forcing, clear-sky longwave radiation, and the sum of sensible and latent heat fluxes during the 1998–2013 are 0.78° ± 0.24°C decade^{-1}, 0.36° ± 0.13°C decade^{-1}, and −0.73° ± 0.17°C decade^{-1}, respectively, indicating that their contributions are detectable. Moreover, results from GEWEX-LPLA and CERES also confirm that contributions from cloud-radiative forcing and clear-sky longwave during 2000–13 are much larger than those during 1984–97. As CMFD/CSSPv2 does not separate clear-sky and cloudy-sky radiation, contributions from total shortwave and longwave radiation are calculated instead. The result shows a larger contribution from shortwave radiation (Tot-SW = CRF-SW + CLR-SW) during 1998–2013 (Fig. S3a), which can be attributed to the cloud-radiative effect because the clear-sky shortwave radiation changes little during this period, as suggested by the results above. Therefore, multisource datasets suggest that cloud-radiative forcing and clear-sky longwave radiation are the main factors for the accelerated warming trend in summer.

For the winter season, the surface upward shortwave radiation shows a large decreasing trend during 1998–2013, whereas its trend is not clear during 1981–97 due to opposite trends in different data (JRA-55 and WRF) (Fig. S2b). Both JRA-55 and WRF simulations show that surface downward cloudy-sky shortwave and longwave radiation change little before and after 1998, while surface downward clear-sky longwave radiation switches from a decreasing trend to an increasing trend (Fig. S2b). However, MERRA shows a large increasing trend in surface downward cloudy-sky shortwave radiation and a small change in surface downward clear-sky longwave radiation (Fig. S2b). We further compare those three datasets with CMFD, and find that JRA-55, WRF, and CMFD all show an increasing trend of longwave radiation but a much smaller changing rate of shortwave radiation (not shown). Thus, MERRA may overestimate the cloudy-sky shortwave radiation changes and underestimate the clear-sky longwave radiation changes. Attribution results show that the surface albedo change is the major factor responsible for the accelerated ground surface warming, with the contribution increasing from −0.38° to −0.16°C decade^{-1} during 1981–97 to 0.94° to 1.15°C decade^{-1} during 1998–2013 (Fig. 5). Chen et al. (2017) find that snow cover is highly correlated with anomalies in surface albedo over TP. Figure S4 shows that winter snow depth averaged over the southeastern TP increases slightly during 1981–97, which increases surface albedo and cools the ground surface. However, the snow depth decreases during 1998–2013, which reduces surface albedo and warms the ground surface. JRA-55 might misrepresent the surface albedo contribution during 1981–97 as it misrepresents the increasing trend of snow depth during 1981–97 (Fig. S4). In addition, both the JRA-55 and WRF datasets show that clear-sky longwave radiation, whose contribution increases from a range of −0.07° to −0.08°C decade^{-1} to a range of 0.41° to 0.47°C decade^{-1} is the second largest warming term during 1998–2013. The attribution result from CMFD/CSSPv2 also suggests that longwave radiation is the second largest warming factor during 1998–2013 (Fig. S3b). Ensemble means of the contribution of surface albedo and longwave radiation shown in Fig. 5 are 1.05° ± 0.1°C decade^{-1} and 0.30° ± 0.25°C decade^{-1}, respectively, indicating that their warming effects are detectable. Thus, surface albedo change and clear-sky longwave radiation are two major factors for the accelerated warming over the southeastern TP during winter.

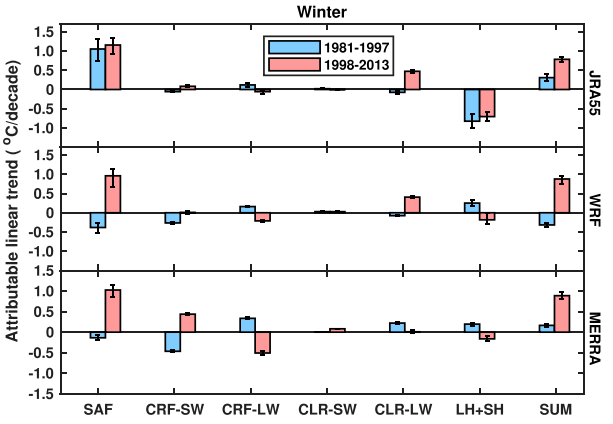

FIG. 5. As in Fig. 4, but for the winter season. Remote sensing–based datasets are not used in winter due to their poor performance (section 3b).

d. *Mechanisms for changes in atmospheric radiative processes*

Considering that the cloud-radiative forcings are directly related to the cloud cover and surface downward cloudy-sky shortwave radiation increases mainly in August (Fig. S5), changes of total cloud fraction in August are shown in Fig. 6. The CDIAC-EECRA observation shows an increasing trend over southeastern TP during 1981–97 and a decreasing trend during 1998–2009 (Figs. 6a,b). Remotely sensed total cloud fraction from the CERES dataset also shows a similar decreasing changing pattern during 2000–13 (Fig. 6c). Thus, a decreasing trend of total cloud cover during 1998–2013 can be inferred from CDIAC-EECRA and CERES.

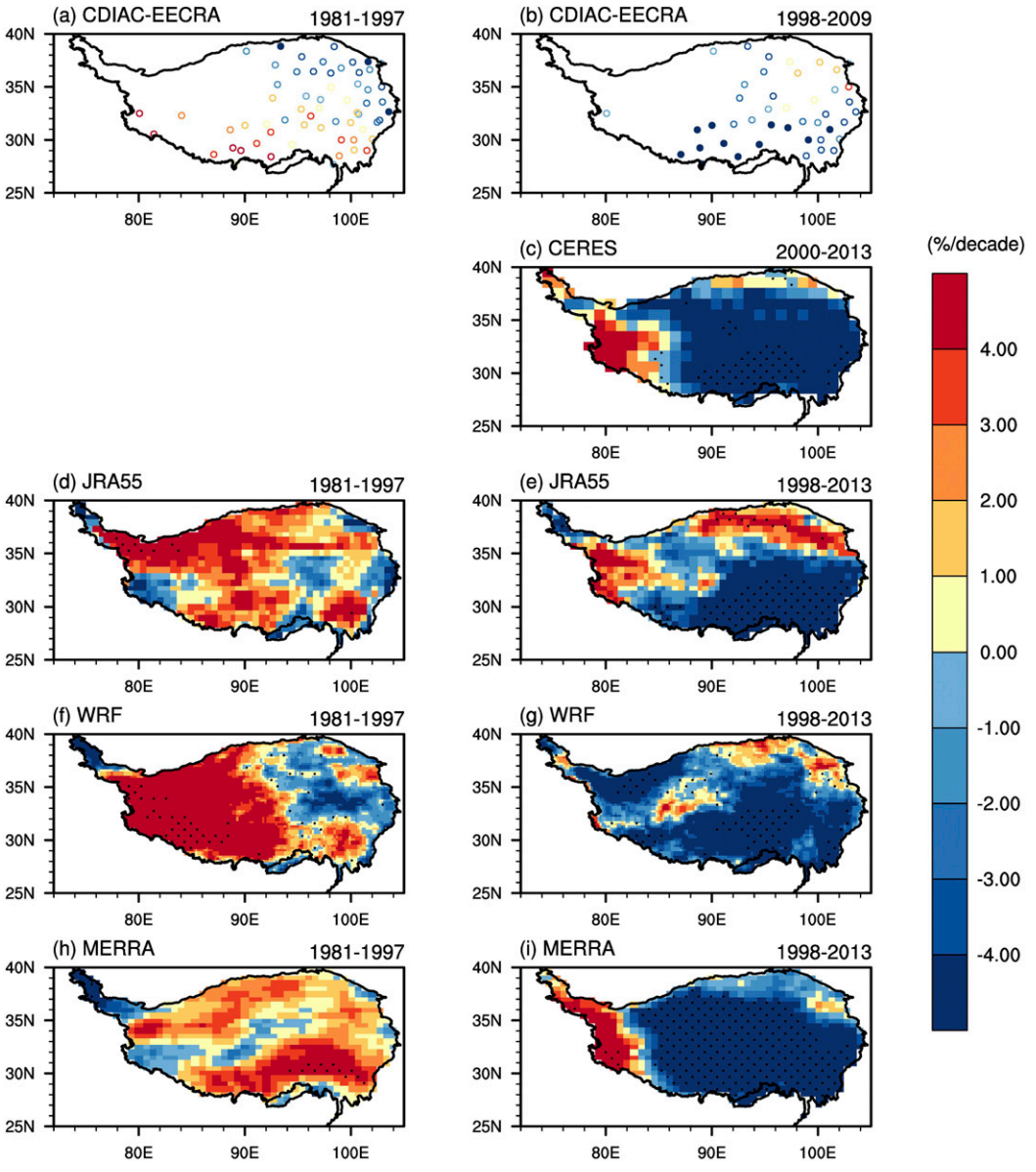

FIG. 6. (a),(b) Linear trends (% decade^{-1}) of observed total cloud fraction in August during 1981–97 and 1998–2009. (c) As in (b), but for remotely sensed total cloud fraction during 2000–13. The remaining panels are as in (a) and (b), but for the (d),(e) JRA-55, (f),(g) WRF, and (h),(i) MERRA datasets, respectively. Solid circles in (a) and (b) represent the 90% significance levels while black dots in (c)–(i) represent the 95% significance levels.

JRA-55, WRF, and MERRA all capture the cloud changes well with significant decreasing trends of total cloud fraction occurring over the southeastern TP (Figs. 6d–i). Correspondingly, the shortwave radiation experiences significantly increasing trends during 1998–2013 while the longwave radiation generally shows smaller and insignificant decreasing trends.

The cloud changes are very complex as cloud formation is affected by changes of atmospheric water vapor, atmospheric vertical motion, and so on. Gao et al. (2014) suggest that large-scale dynamic circulation change is a major cause of drying over the southeastern TP in wet seasons. To further investigate impacts of large-scale circulation, the integrated water vapor flux (WVF) is regressed to the normalized mean cloud fraction over the southeastern TP during the Augusts of 1981–2013, 1981–97, and 1998–2013, respectively. Figures 7a–c show that cloud fraction over the southeastern TP is significantly related to the southwestern water vapor flux in the region to the south of the TP (red lines in Fig. 7;

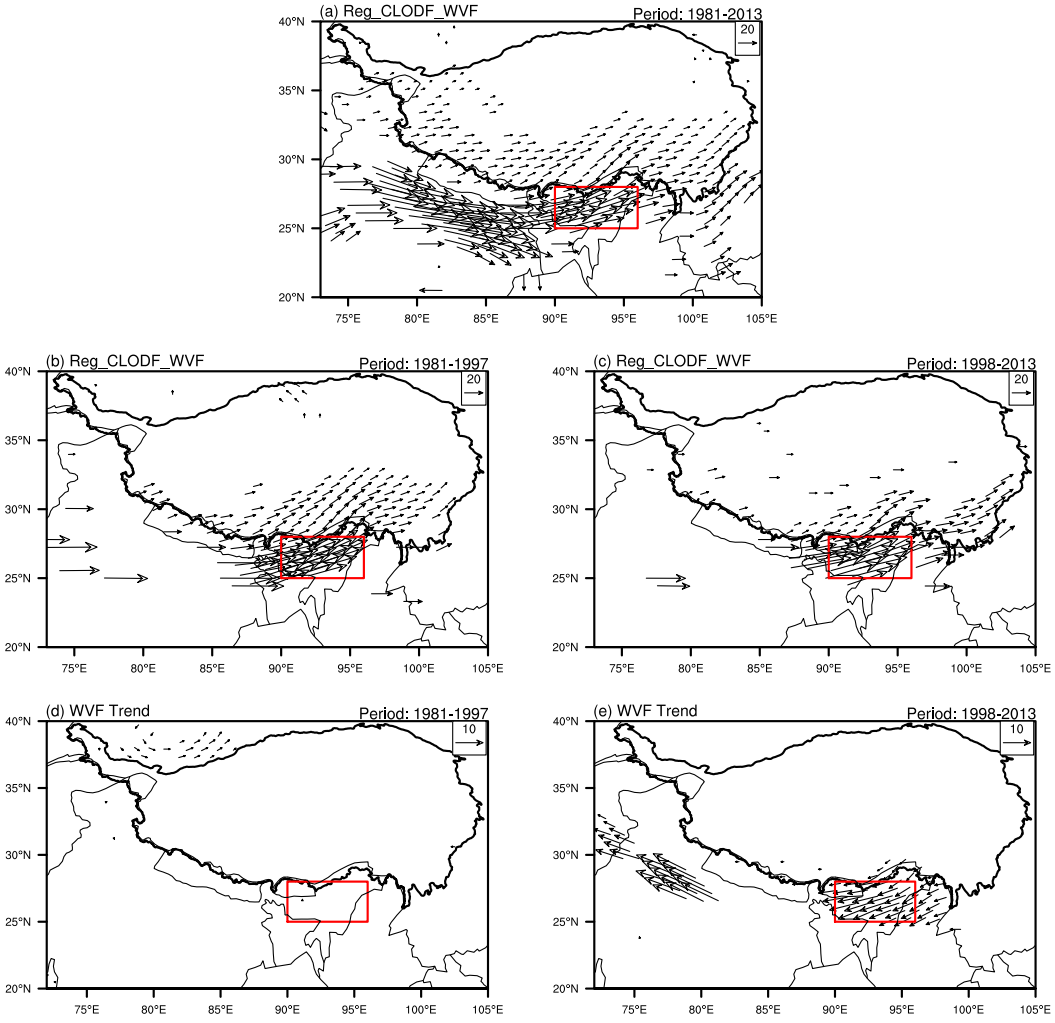

FIG. 7. (a)–(c) Regressions of integrated water vapor flux (WVF) to the mean total cloud fraction averaged over the southeastern TP during 1981–2013, 1981–97, and 1998–2013, respectively. (d),(e) WVF changes during 1981–97 and 1998–2013, respectively. Only the significant ($p < 0.1$) results are shown here.

25°–28°N, 90°–96°E) during all three periods. Figure 7d shows that there is no significant change in water vapor flux during 1981–97, which is consistent with the insignificant change of cloud fraction over the southeastern TP. However, Fig. 7e shows that significant northeastern water vapor flux occurs over the region to the south of the TP shown by red lines during 1998–2013, indicating that less water vapor can be transported into the southeastern TP. Only the result of JRA-55 is shown in Fig. 7, considering that results from MERRA and WRF datasets are similar.

The black line in Fig. 8a shows the variation of South Asian summer monsoon (SASM) index during the August of 1981–2013. The SASM index is defined as the differences between 850- and 200-hPa zonal winds averaged in the region covering 0°–20°N, 40°–100°E following Sun et al. (2010). There is generally no linear trend in SASM index during 1981–97, whereas a significant decreasing trend ($p = 0.06$) occurs during 1998–2013. As the SASM circulation brings sufficient water vapor to the south of the TP through southwest wind (vectors in Fig. 8b) and has significantly positive correlation with the total cloud fraction over the south of the TP (shaded regions in Fig. 8b), weakening of the SASM will cause a northeast anomaly in water vapor flux (Fig. 7e) and thus suppress cloud formation over the southeastern TP. This is also confirmed by the significant correlation between the SASM index and mean cloud fraction over the southeastern TP (Fig. 8a).

Different from large-scale circulation, which mainly supplies water vapor for TP, local-scale circulation directly controls the cloud formation through local

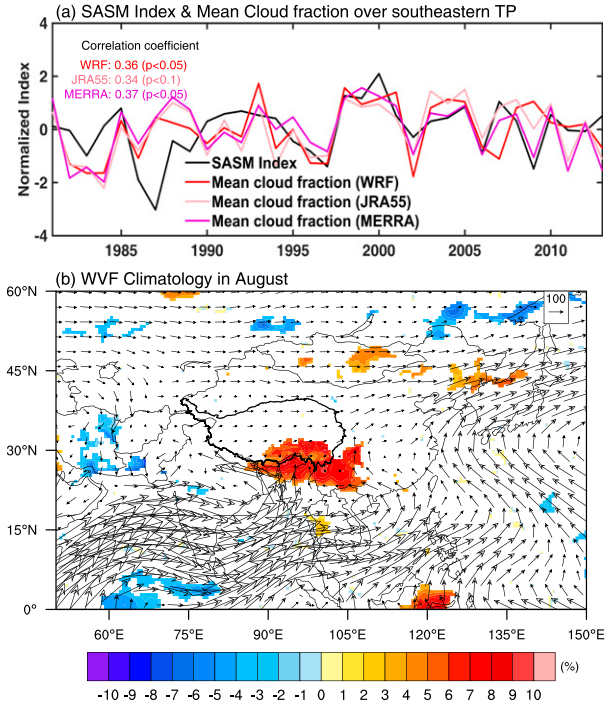

FIG. 8. (a) Time series of normalized South Asian summer monsoon (SASM) index and normalized total cloud fraction averaged over the southeastern TP. (b) Climatology of water vapor flux in August during 1981–2013 (vectors) and the regression of total cloud fraction to the SASM index during 1998–2013 (shaded regions). Only significant ($p < 0.1$) regression results are shown here. The JRA-55 dataset is used here; similar patterns can be found in WRF and MERRA.

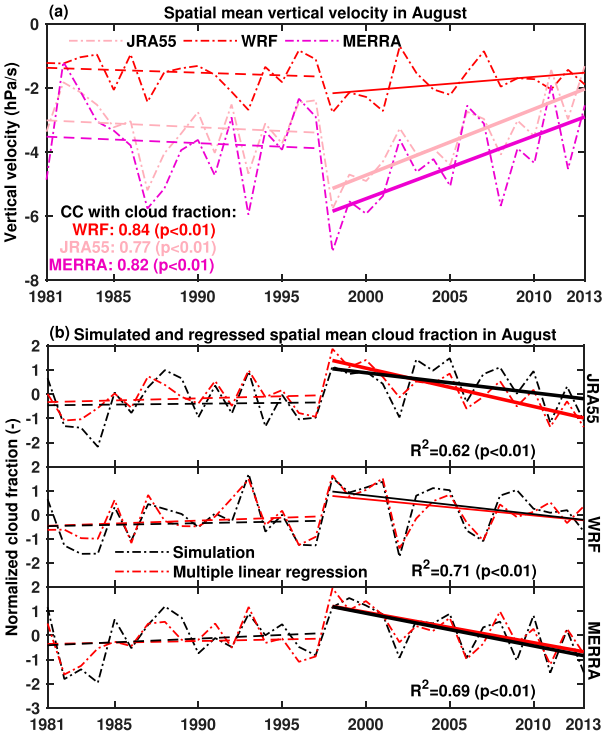

FIG. 9. (a) Spatial mean vertical velocity at 500-hPa level over the southeastern TP and its correlation coefficient (CC) with spatial mean total cloud fraction. (b) Simulated (black dash–dotted line) and multiple-linear-regressed (red dash–dotted line) normalized total cloud fraction over the southeastern TP. Normalized spatial mean vertical velocity and normalized SASM are used to construct a multiple linear regression function of normalized cloud fraction. Dashed straight lines represent linear regression with insignificant trends, while thin and thick straight lines represent linear regressions with 90% and 95% confidence levels, respectively.

atmospheric vertical motion. Figure 9a shows that the correlation coefficient between vertical velocities (hPa s^{-1}) at 500 hPa and total cloud fraction can reach up to 0.84. Figure 9a also shows that vertical upward motion changes from an insignificant increasing trend during 1981–97 to a significant decreasing trend during 1998–2013, which is consistent with cloud fraction changes shown in Fig. 8a. Multiple linear regression results show that SASM and local vertical velocity can interpret 62%–71% of the variance of cloud fraction during 1981–2013 (Fig. 9b). Regression results also reproduce the significant decreasing trend of total cloud during 1981–2013, which is about 0.86–1.9 times the simulated one. Moreover, 10%–13% of the reproduced decreasing trend is caused by the SASM term while the remainder of the trend is caused by the vertical motion term. Thus, both a large circulation change and local vertical motion change led to the decreasing trend of total cloud in 1981–2013, with the latter playing a dominant role.

For the clear-sky longwave radiation in winter, previous research finds it positively correlated with the water vapor amount in the atmosphere (or precipitable water) over highland regions including the TP (Naud et al. 2012), indicating that the increasing clear-sky longwave radiation may be caused by the increased precipitable water. However, as revealed by the JRA-55 and WRF datasets, both summer and winter precipitable water do not increase significantly and even decrease during 1998–2013 (Fig. 10). Note that the MERRA dataset is not used here because it cannot capture the increased clear-sky longwave radiation in winter (see section 3c). No matter which dataset is used, changes in water vapor alone cannot explain the increasing trend of clear-sky longwave radiation over the southeastern TP. In addition to the water vapor amount, the clear-sky longwave radiation is also strongly dependent on the temperature profile. We find that the middle to upper troposphere (500–200 hPa) switches from a cooling trend during 1981–97 to a warming trend during 1998–2013 over the southeastern TP both in summer and winter (Fig. 11), which may be responsible for the increased clear-sky longwave radiation.

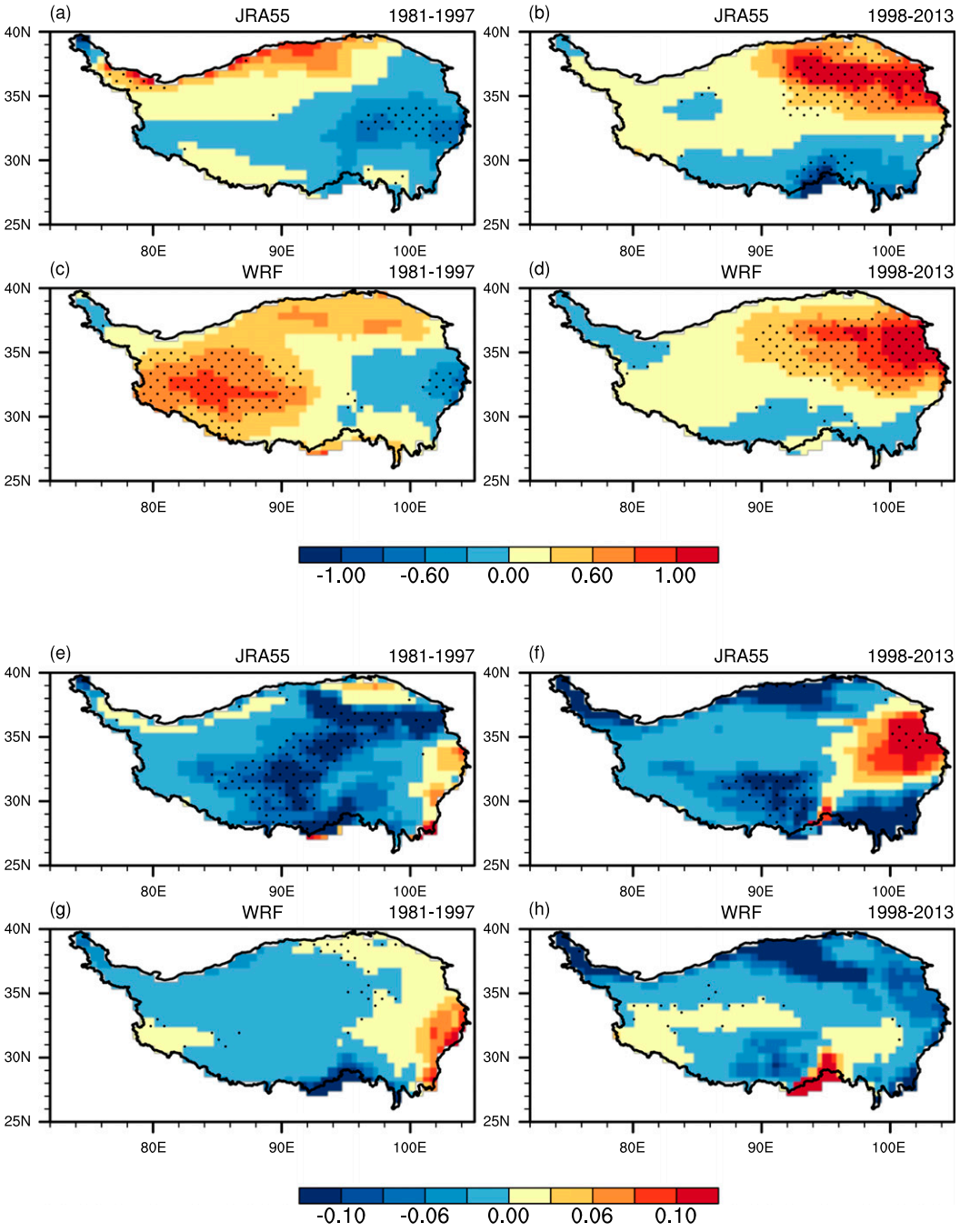

FIG. 10. (a),(b) Precipitable water changes (mm yr^{-1}) in winter during 1981–97 and 1998–2013 simulated by JRA-55, with black dots showing regions with significant ($p < 0.1$) trends. (c),(d) As in (a) and (b), but for the WRF simulation. (e)–(h) As in (a)–(d), respectively, but for winter.

To further quantify the impact of water vapor amount and temperature profile on the clear-sky longwave radiation in winter, we use precipitable water and air temperature at different layers in the troposphere to fit a simple linear stepwise regression model for the clear-sky longwave radiation, and estimate their contributions using the differential form of the fitted function (see section 2d for details). The stratosphere is not considered because of the long distance from ground and its cooling effect on the ground surface during 2000–09 (Solomon et al. 2010). Although the simple stepwise regression only considers two factors, the fitted model

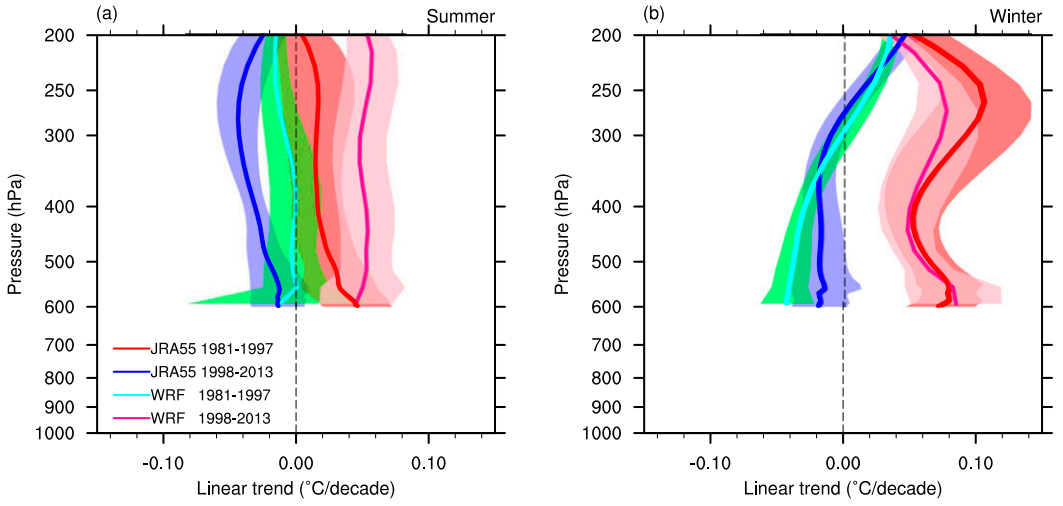

FIG. 11. (a) Changes of air temperature (°C decade^{-1}) in summer at different atmospheric layers averaged for 78 stations over the southeastern TP from JRA-55 and WRF during 1981–97 and 1998–2013, with the shaded areas showing one standard deviation. (b) As in (a), but for winter.

explains about 98%–99% of the total variance of the clear-sky longwave radiation, with a root-mean-square error (RMSE) of only 4–5 W m^{-2}. Moreover, the estimated clear-sky longwave radiation change is consistent with the results from WRF simulation and reanalysis (Fig. 12). Positive contributions from air temperature can be found both in summer (Figs. 12a,b) and winter (Figs. 12c,d), and are more robust in winter as the temperature-caused terms are significantly above zero. Contributions from precipitable water are smaller and have larger uncertainties that may come from the heterogeneous changing patterns. These results confirm that increasing clear-sky longwave radiation over the southeastern TP in summer and winter is mainly due to the warming in the middle to upper troposphere instead of precipitable water changes.

4. Conclusions and discussion

Our results explain the accelerated ground surface warming trend over the southeastern TP during 1998–2013 from the energy balance perspective by quantifying the contributions of different processes. Surface albedo and cloud-radiative forcing are found to play the most important role in winter and summer, respectively. This is an important complement to the previous studies, which emphasized surface albedo changes (Ghatak et al. 2014; He et al. 2018; Ramanathan and Carmichael 2008) or cloud process (Duan and Xiao 2015). Moreover, we find that clear-sky longwave radiation is also a vital factor in both winter and summer for the TP, as it contributes about 21%–48% to the accelerated ground surface warming. Our results are consistent with a previous study highlighting the important warming effects of longwave radiation over the Arctic (Kim and Kim 2017). However, different from the Arctic where precipitable water is increasing (Kim and Kim 2017), the southeastern TP experiences slightly changes in precipitable water. The increased clear-sky longwave radiation in the southeastern TP is mainly controlled by the warming middle to upper troposphere instead of the precipitable water. Our results emphasize the importance of atmospheric radiative processes (such as cloud radiative effects and clear-sky longwave radiation) in the accelerated ground surface warming in the southeastern TP. Improving the parameterizations of cloud and clear-sky longwave radiation may improve model ability in simulating the warming environment and the corresponding hydrological, ecological, and cryospheric changes over the southeastern TP.

Previous work suggested that radiative forcing of greenhouse gases can lead to a warming upper troposphere (IPCC 1996). In addition, the increased turbulent fluxes during 1998–2013 (Figs. S2 and S4) can also lead to a strong boundary layer heating and cause a warming middle to upper troposphere through the resultant atmospheric thermal adaptation and overshooting (Duan et al. 2006). However, a warming middle to upper troposphere is also found over southeastern China (Fig. S6) where ground surface cooling happens and turbulent fluxes change little, indicating that this phenomenon is mainly induced by the large-scale increasing trend of greenhouse gases. Further efforts are needed to understand the interactions between

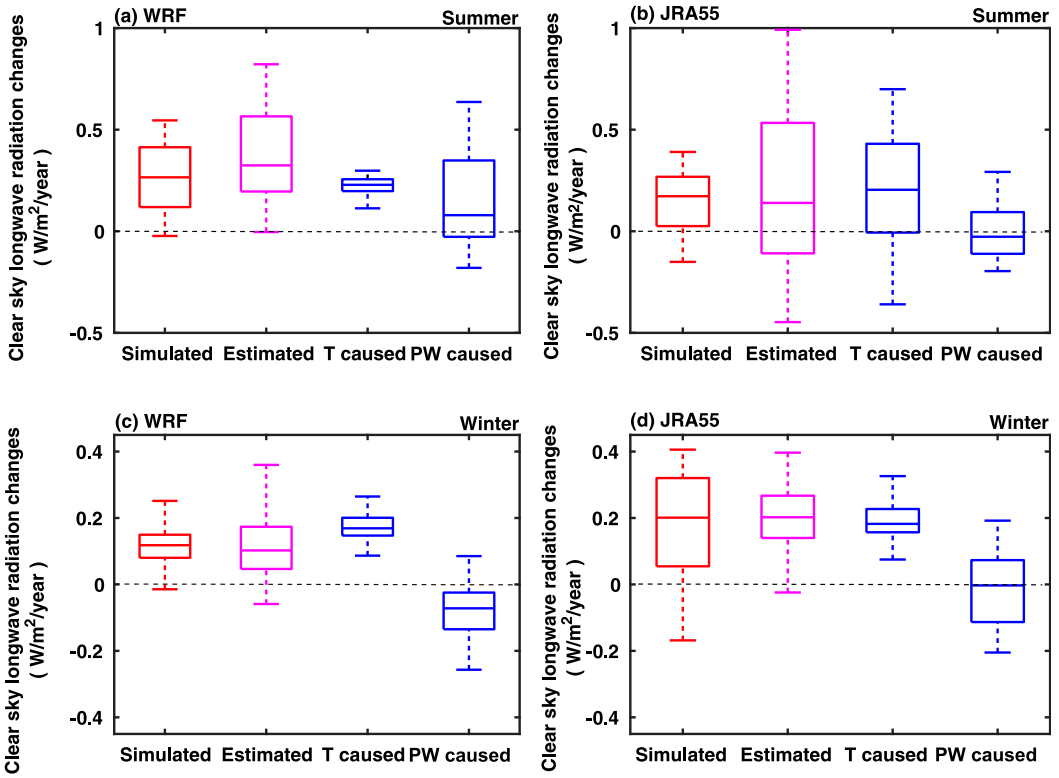

FIG. 12. Trends for simulated and linear-stepwise-regressed clear-sky longwave changes for 78 stations over the southeastern TP in (a),(b) summer and (c),(d) winter during 1998–2013 based on the WRF and JRA-55 datasets. Trends caused by air temperature and precipitable water (PW) are also shown separately. (c),(d) As in (a) and (b), but for stations over SE China. Solid lines in boxes show median values, boxes show the 25th and 75th percentiles, and dashed lines show the whole range.

those processes and quantitatively analyze their contributions.

We do not include the northeastern TP in this research as current datasets cannot capture the ground surface warming over the region during 1998–2013. Duan and Xiao (2015) suggest that cloud fraction in nighttime has a larger increasing trend than that in daytime, which may lead to continued warming over the northeastern TP through enhanced atmospheric counterradiation. Ji and Yuan (2020) show that reanalysis datasets and WRF simulation underestimate the increasing trends of nighttime cloud fraction over the northeastern TP, which may be the reason for the insignificant ground warming trends in those datasets. Further efforts should be paid to diagnosing the causes of surface warming over the northeastern TP. Moreover, the significant warming during spring is not captured by current datasets; possible reasons for this require further work.

Our results also show that not all reanalysis datasets capture the accelerated ground warming over the southeastern TP. During the summer season of 1998–2013, ERA-Interim overestimates the increasing trend of upward shortwave radiation and underestimates the increasing trend of clear-sky downward longwave radiation compared with WRF simulation (Figs. S7 and S2). MERRA2 underestimates the increasing trend of cloudy-sky shortwave radiation as compared with MERRA. During the winter season of 1998–2013 (Fig. S7), a large negative trend of cloudy-sky longwave radiation in CERES may be caused by uncertainties in the input data sources, a large adjustment of surface flux over TP, and a switch of geostationary satellites (Kato et al. 2018). ERA-Interim, MERRA2, and CERES miss the decreasing trend of upward shortwave radiation, which is contrary to the datasets shown in Fig. S4 and previous research (Chen et al. 2017). Thus, the representation of changes in surface albedo, cloud shortwave radiative forcing, and clear-sky longwave radiation over highland areas needs to be improved in global climate models. The WRF regional climate modeling significantly improves the simulations compared to the ERA-Interim global dataset, which is used to provide boundary conditions for WRF, indicating the necessity

of high-resolution modeling over the TP and potentially other highland areas (Gao et al. 2014).

Although the contributions of different processes are generally consistent among different datasets, there are still some uncertainties. For example, there are underestimations of the warming trends from the selected gridded datasets, and the estimated warming trend by Eq. (3) is not exactly the same as the observed trend. Multimodel comparison or superensemble simulations by using the WRF Model could be used to better quantify these uncertainties.

Acknowledgments. This work was supported by National Key R&D Program of China (2018YFA0606002), the National Natural Science Foundation of China (41875105, 91547103), and the Startup Foundation for Introducing Talent of NUIST. Ground temperature observations are provided by CMA (http://data.cma.cn/en). The JRA-55 comes from the Japan Meteorological Agency (http://www.jma.go.jp/jma/); the MERRA, GEWEX-LPLA and CERES datasets come from the National Aeronautics and Space Administration (NASA) (https://gmao.gsfc.nasa.gov/); and ERA-Interim comes from the European Center for Medium-Range Weather Forecasts (https://www.ecmwf.int/). The GEWEX-SRB and GEWEX-LPLA datasets are provided by NASA (https://eosweb.larc.nasa.gov/project/srb/srb_table). ISCCP-FD and CERES come from the ISCCP website (https://isccp.giss.nasa.gov/products/products.html#fd) and CERES website (https://ceres.larc.nasa.gov/index.php) respectively. The authors declare no competing interests.

REFERENCES

Bird, P., and M. Toksöz, 1977: Strong attenuation of Rayleigh waves in Tibet. *Nature*, **266**, 161–163, https://doi.org/10.1038/266161a0.

Brown, P. J., and A. T. DeGaetano, 2011: A paradox of cooling winter soil surface temperatures in a warming northeastern United States. *Agric. For. Meteor.*, **151**, 947–956, https://doi.org/10.1016/j.agrformet.2011.02.014.

Chen, X., D. Long, Y. Hong, S. Liang, and A. Hou, 2017: Observed radiative cooling over the Tibetan Plateau for the past three decades driven by snow cover-induced surface albedo anomaly. *J. Geophys. Res.*, **122**, 6170–6185, https://doi.org/10.1002/2017JD026652.

Dee, D. P., and Coauthors, 2011: The ERA-Interim reanalysis: Configuration and performance of the data assimilation system. *Quart. J. Roy. Meteor. Soc.*, **137**, 553–597, https://doi.org/10.1002/qj.828.

Dehecq, A., and Coauthors, 2019: Twenty-first century glacier slowdown driven by mass loss in High Mountain Asia. *Nat. Geosci.*, **12**, 22–27, https://doi.org/10.1038/s41561-018-0271-9.

Duan, A., and G. X. Wu, 2009: Weakening trend in the atmospheric heat source over the Tibetan Plateau during recent decades. Part II: Connection with climate warming. *J. Climate*, **22**, 4197–4212, https://doi.org/10.1175/2009JCLI2699.1.

——, and Z. Xiao, 2015: Does the climate warming hiatus exist over the Tibetan Plateau? *Sci. Rep.*, **5**, 13711, https://doi.org/10.1038/srep13711.

——, G. X. Wu, Q. Zhang, and Y. M. Liu, 2006: New proofs of the recent climate warming over the Tibetan Plateau as a result of the increasing greenhouse gases emissions. *Chin. Sci. Bull.*, **51**, 1396–1400, https://doi.org/10.1007/s11434-006-1396-6.

Fang, X., S. Luo, and S. Lyu, 2019: Observed soil temperature trends associated with climate change in the Tibetan Plateau, 1960–2014. *Theor. Appl. Climatol.*, **135**, 169–181, https://doi.org/10.1007/s00704-017-2337-9.

Gao, Y., L. Cuo, and Y. Zhang, 2014: Changes in moisture flux over the Tibetan Plateau during 1979–2011 and possible mechanisms. *J. Climate*, **27**, 1876–1893, https://doi.org/10.1175/JCLI-D-13-00321.1.

Garcia-Pichel, F., V. Loza, Y. Marusenko, P. Mateo, and R. M. Potrafka, 2013: Temperature drives the continental-scale distribution of key microbes in topsoil communities. *Science*, **340**, 1574–1577, https://doi.org/10.1126/science.1236404.

Gelaro, R., and Coauthors, 2017: The Modern-Era Retrospective Analysis for Research and Applications, version 2 (MERRA-2). *J. Climate*, **30**, 5419–5454, https://doi.org/10.1175/JCLI-D-16-0758.1.

Ghatak, D., E. Sinsky, and J. Miller, 2014: Role of snow-albedo feedback in higher elevation warming over the Himalayas, Tibetan Plateau and Central Asia. *Environ. Res. Lett.*, **9**, 114008, https://doi.org/10.1088/1748-9326/9/11/114008.

Gupta, S. K., D. P. Kratz, P. W. Stackhouse Jr., and A. C. Wilber, 2001: The Langley Parameterized Shortwave Algorithm (LPSA) for surface radiation budget studies (version 1.0). NASA/TP-2001-211272, 31 pp.

Hahn, C. J., S. G. Warren, and R. Eastman, 1999: Extended edited synoptic cloud reports from ships and land stations over the globe, 1952–1996. Carbon Dioxide Information Analysis Center, accessed June 2018, https://doi.org/10.3334/CDIAC/CLI.NDP026C.

He, C., M. G. Flanner, F. Chen, M. Barlage, K. N. Liou, S. Kang, J. Ming, and Y. Qian, 2018: Black carbon-induced snow albedo reduction over the Tibetan Plateau: Uncertainties from snow grain shape and aerosol–snow mixing state based on an updated SNICAR model. *Atmos. Chem. Phys.*, **18**, 11 507–11 527, https://doi.org/10.5194/acp-18-11507-2018.

He, J., and K. Yang, 2011: China meteorological forcing dataset. Cold and Arid Regions Science Data Center, accessed January 2018, https://doi.org/10.3972/westdc.002.2014.db.

IPCC, 1996: *Climate Change 1995: The Science of Climate Change*. J. T. Houghton et al., Eds., Cambridge University Press, 362 pp.

Ji, P., and X. Yuan, 2018: High-resolution land surface modeling of hydrological changes over the Sanjiangyuan region in the eastern Tibetan Plateau: 2. Impact of climate and land cover change. *J. Adv. Model. Earth Syst.*, **10**, 2829–2843, https://doi.org/10.1029/2018MS001413.

——, and ——, 2020: Underestimation of warming trend over Tibetan Plateau during 1998–2013 by global land data assimilation systems and atmospheric reanalysis. *J. Meteor. Res.*, in press.

Kato, S., and Coauthors, 2018: Surface irradiances of Edition 4.0 Clouds and the Earth's Radiant Energy System (CERES) Energy Balanced and Filled (EBAF) data product. *J. Climate*, **31**, 4501–4527, https://doi.org/10.1175/JCLI-D-17-0523.1.

Kim, H. M., and B. M. Kim, 2017: Relative contributions of atmospheric energy transport and sea ice loss to the recent warm Arctic winter. *J. Climate*, **30**, 7441–7450, https://doi.org/10.1175/JCLI-D-17-0157.1.

Kobayashi, S., and Coauthors, 2015: The JRA-55 reanalysis: General specifications and basic characteristics. *J. Meteor. Soc. Japan*, **93**, 5–48, https://doi.org/10.2151/jmsj.2015-001.

Kosaka, Y., and S. P. Xie, 2013: Recent global-warming hiatus tied to equatorial Pacific surface cooling. *Nature*, **501**, 403–407, https://doi.org/10.1038/nature12534.

Koven, C. D., G. Hugelius, D. M. Lawrence, and W. R. Wieder, 2017: Higher climatological temperature sensitivity of soil carbon in cold than warm climates. *Nat. Climate Change*, **7**, 817–822, https://doi.org/10.1038/nclimate3421.

Lesins, G., T. J. Duck, and J. R. Drummond, 2012: Surface energy balance framework for Arctic amplification of climate change. *J. Climate*, **25**, 8277–8288, https://doi.org/10.1175/JCLI-D-11-00711.1.

Lin, H., and Z. Wu, 2011: Contribution of the autumn Tibetan Plateau snow cover to seasonal prediction of North American winter temperature. *J. Climate*, **24**, 2801–2813, https://doi.org/10.1175/2010JCLI3889.1.

Lu, J. H., and M. Cai, 2009: Seasonality of polar surface warming amplification in climate simulations. *Geophys. Res. Lett.*, **36**, L16704, https://doi.org/10.1029/2009GL040133.

Ma, Z., W. Zhao, M. Liu, and Q. Liu, 2018: Responses of soil respiration and its components to experimental warming in an alpine scrub ecosystem on the eastern Qinghai-Tibet Plateau. *Sci. Total Environ.*, **643**, 1427–1435, https://doi.org/10.1016/j.scitotenv.2018.06.243.

Medhaug, I., M. B. Stolpe, E. M. Fischer, and R. Knutti, 2017: Reconciling controversies about the 'global warming hiatus.' *Nature*, **545**, 41–47, https://doi.org/10.1038/nature22315.

Naud, C. M., J. R. Miller, and C. Landry, 2012: Using satellites to investigate the sensitivity of longwave downward radiation to water vapor at high elevations. *J. Geophys. Res.*, **117**, D05101, https://doi.org/10.1029/2011JD016917.

Pinker, R. T., and I. Laszlo, 1992: Modeling surface solar irradiance for satellite applications on a global scale. *J. Appl. Meteor.*, **31**, 194–211, https://doi.org/10.1175/1520-0450(1992)031<0194:MSSIFS>2.0.CO;2.

Qiu, J., 2008: China: The third pole. *Nature*, **454**, 393–396, https://doi.org/10.1038/454393a.

Ramanathan, V., and G. Carmichael, 2008: Global and regional climate changes due to black carbon. *Nat. Geosci.*, **1**, 221–227, https://doi.org/10.1038/ngeo156.

Rienecker, M. R., and Coauthors, 2011: MERRA-NASA's Modern-Era Retrospective Analysis for Research and Applications. *J. Climate*, **24**, 3624–3648, https://doi.org/10.1175/JCLI-D-11-00015.1.

Skamarock, W. C., J. B. Klemp, J. Dudhia, D. O. Barker, M. G. Duda, X. Huang, W. Wang, and J. G. Powers, 2008: A description of the Advanced Research WRF version 3. NCAR Tech. Note NCAR/TN-475+STR, 113 pp., https://doi.org/10.5065/D68S4MVH.

Solomon, S., K. H. Rosenlof, R. W. Portmann, J. S. Daniel, S. M. Davis, T. J. Sanford, and G. Plattner, 2010: Contributions of stratospheric water vapor to decadal changes in the rate of global warming. *Science*, **327**, 1219–1223, https://doi.org/10.1126/science.1182488.

Sun, Y., Y. Ding, and A. Dai, 2010: Changing links between South Asian summer monsoon circulation and tropospheric land–sea thermal contrasts under a warming scenario. *Geophys. Res. Lett.*, **37**, L02704, https://doi.org/10.1029/2009GL041662.

Wang, L., M. Henderson, B. Liu, X. Shen, X. Chen, L. Lian, and D. Zhou, 2018: Maximum and minimum soil surface temperature trends over China, 1965–2014. *J. Geophys. Res.*, **123**, 2004–2016, https://doi.org/10.1002/2017JD027283.

Woodbury, A. D., A. K. M. H. Bhuiyan, J. Hanesiak, and O. O. Akinremi, 2009: Observations of northern latitude ground-surface and surface-air temperatures. *Geophys. Res. Lett.*, **36**, L07703, https://doi.org/10.1029/2009GL037400.

Xie, S.-P., and Y. Kosaka, 2017: What caused the global surface warming hiatus of 1998–2013? *Curr. Climate Change Rep.*, **3**, 128–140, https://doi.org/10.1007/s40641-017-0063-0.

Xue, Y., Y. Ma, and Q. Li, 2017: *Land–Climate Interaction over the Tibetan Plateau*. Oxford Research Encyclopedias: Climate Science, https://doi.org/10.1093/acrefore/9780190228620.013.592.

Yang, K., R. T. Pinker, Y. Ma, T. Koike, M. M. Wonsick, S. J. Cox, Y. Zhang, and P. Stackhouse, 2008: Evaluation of satellite estimates of downward shortwave radiation over the Tibetan Plateau. *J. Geophys. Res.*, **113**, D17204, https://doi.org/10.1029/2007JD009736.

——, H. Wu, J. Qin, C. Lin, W. Tang, and Y. Chen, 2014: Recent climate changes over the Tibetan Plateau and their impacts on energy and water cycle: A review. *Global Planet. Change*, **112**, 79–91, https://doi.org/10.1016/j.gloplacha.2013.12.001.

Yang, M., F. E. Nelson, N. I. Shiklomanov, D. Guo, and G. Wan, 2010: Permafrost degradation and its environmental effects on the Tibetan Plateau: A review of recent research. *Earth-Sci. Rev.*, **103**, 31–44, https://doi.org/10.1016/j.earscirev.2010.07.002.

Yao, T., and Coauthors, 2012: Third Pole Environment (TPE). *Environ. Dev.*, **3**, 52–64, https://doi.org/10.1016/j.envdev.2012.04.002.

Yuan, X., P. Ji, L. Wang, X.-Z. Liang, K. Yang, A. Ye, Z. Su, and W. Jun, 2018: High-resolution land surface modeling of hydrological changes over the Sanjiangyuan region in the eastern Tibetan Plateau: 1. Model development and evaluation. *J. Adv. Model. Earth Syst.*, **10**, 2806–2828, https://doi.org/10.1029/2018MS001412.

Zhang, H., E. Wang, D. Zhou, Z. Luo, and Z. Zhang, 2016: Rising soil temperature in China and its potential ecological impact. *Sci. Rep.*, **6**, 35530, https://doi.org/10.1038/srep35530.

Zhang, Y., W. B. Rossow, A. A. Lacis, V. Oinas, and M. I. Mishchenko, 2004: Calculation of radiative fluxes from the surface to top of atmosphere based on ISCCP and other global data sets: Refinements of the radiative transfer model and the input data. *J. Geophys. Res.*, **109**, D19105, https://doi.org/10.1029/2003JD004457.

Zhu, F., L. Cuo, Y. Zhang, J. J. Luo, D. P. Lettenmaier, Y. Lin, and Z. Liu, 2018: Spatiotemporal variations of annual shallow soil temperature on the Tibetan Plateau during 1983–2013. *Climate Dyn.*, **51**, 2209–2227, https://doi.org/10.1007/s00382-017-4008-z.

Zhu, L., G. Huang, G. Fan, X. Qu, G. Zhao, and W. Hua, 2017: Evolution of surface sensible heat over the Tibetan Plateau under the recent global warming hiatus. *Adv. Atmos. Sci.*, **34**, 1249–1262, https://doi.org/10.1007/s00376-017-6298-9.